



# Magnetic and Mössbauer study of lanthanum-doped nanosized cobalt ferrite assembly

Meenal Gupta<sup>1</sup> · Anusree Das<sup>2</sup> · Satyabrata Mohapatra<sup>1</sup> · Dipankar Das<sup>2</sup> · Saurav Dutta<sup>3</sup> · Anindya Datta<sup>1</sup>

Received: 14 February 2023 / Accepted: 5 December 2023 / Published online: 2 January 2024  
© The Author(s), under exclusive licence to Springer-Verlag GmbH, DE part of Springer Nature 2024

## Abstract

Nanoparticles of cobalt ferrite are doped with multiple lanthanum (La) amounts up to an unusually high level of doping. They are synthesised using a soft chemical approach. The structural characterisation is conducted using X-ray diffraction (XRD) and transmission electron microscopy (TEM). The crystallite size, micro strain, crystal density, deformation and twin fault probability are found out by Rietveld analysis. Room temperature Mössbauer spectroscopy is performed for determination of spin aberration due to La doping. The values of isomeric shift are obtained in the range of 0.33–0.41 mm/s for different samples as compared to the standard range of 0.32–0.34 mm/s. Large and narrow hysteresis are observed in 5 K and 300 K magnetic measurements, respectively with coercivities in the range 0.2–2 kOe at room temperature. The coercivity is in the range of 0.8–15 kOe at 5 K. The results from magnetic measurement show deviation from standard which is also seen from the inferences from Photoluminescence (PL) which hint at the increased versatility of the ferrite material by doping with rare earth (RE) metals. However, there is an upper limit to this inclusion in the ferrite matrix. As such there is also the existence of wasp-waist hysteresis which is indicative of antiferromagnetic (AFM) to ferromagnetic (FM) interaction but from the Rietveld analysis it is seen that this coupling does not have an undesirable effect on the stability of the nanoferrite.

**Keywords** Cobalt ferrite · Lanthanum · Photoluminescence · Magnetic · Mössbauer

## 1 Introduction

Ferrite magnetic nanoparticles are materials of significance in extensive areas of research and technology such as bio-medicine, electronics, data storage, catalysis amongst others. When their particle sizes in the range of 10–20 nm, they are critical particle sizes because then these nanoparticles show superparamagnetism (SPM) where the spinel ferrites act as single domains with considerably high magnetic moment but negligible coercivity eliciting fast magnetic response for applications in magnetocaloric refrigeration and nanomagnetism amongst others [1, 2]. Cobalt ferrite magnetic nanoparticles have high coercivities ( $H_c$ ) and retentivities ( $M_r$ ) as well as saturation magnetisation ( $M_s$ ) which leads to a large hysteresis for which the strength of coupling between cobaltous ion at the octahedral and ferric ions at the tetrahedral interstices is the main driving factor. This highly magnetic material has been synthesised using various methods [3–7] for applications based on electronics, spintronics, magnetic refrigeration, ferrofluids, magnetic resonance imaging, and anti-tumour drug delivery [8, 9]. Studies on the impact of dimensions and morphology of the material on its magnetic

---

✉ Anindya Datta  
anindya\_datta@yahoo.com

Meenal Gupta  
meenal\_garg04@hotmail.com

Anusree Das  
anusreedas8@gmail.com

Satyabrata Mohapatra  
smiuc@gmail.com

Dipankar Das  
ddas.ugcdae@gmail.com

Saurav Dutta  
saudatta@gmail.com

<sup>1</sup> University School of Basic and Applied Sciences, Guru Gobind Singh Indraprastha University, Dwarka, New Delhi 110078, India

<sup>2</sup> UGC-DAE Consortium for Scientific Research, Kolkata Centre, Saltlake, Sector-III, LB-8, Kolkata 700106, India

<sup>3</sup> Department of Physics, Rammohan College, 102/1, Raja Rammohan Roy Sarani, Kolkata, West Bengal, India

response have been performed to determine the related properties [10–13]. Spinel ferrites are known for highly stable structures that makes them important materials in diagnosis, drug delivery and even in water purification [14, 15]. The three broad types of spinel structures i.e. mixed, inverse and normal exist based on distributions of the trivalent ferric cation and divalent metal cation in the tetrahedral (A) and the octahedral (B) interstices of the ferrite structure [16, 17]. Cobalt ferrite is known to be an inverse spinel crystal with distribution of  $\text{Co}^{2+}$  and  $\text{Fe}^{3+}$  positively charged ions at A and B sites with general formula  $\text{Fe}^{3+}_A(\text{Co}^{2+}\text{Fe}^{3+})_B\text{O}_4$  [10].

Ongoing research work is being carried out to manipulate and customise the magnetic, electric, and mechanical properties by replacing ferric ion with other trivalent metal ions in cobalt ferrite. Amongst them, modification of ferrites in particular by doping with rare earth (RE) metals has gained popularity and is being extensively explored [18–20]. The primary cause of magnetism in ferrites is spin coupling of d-orbital electrons of iron. In mixed iron oxides such as cobalt ferrite, ferrimagnetism is a consequence of exchange interaction amongst the unequal magnetic dipole moments of A and B sub lattice sites [21]. In case of RE lanthanides, the magnetic moments vary from 0 (La) to 10.5 (Dy) Bohr magneton and the effect of this on the entire material is different in each case. This is because the f-electrons which are the valence electrons for RE elements contribute differently to the interaction with valence electrons of other orbitals of other elements or compounds. In the case of ferrites where the valence electrons come from d-orbitals, this inclusion of lanthanides and actinides into the ferrite matrix causes the 3d-4f coupling due to involvement of 4f electrons of RE dopants which greatly affects the magnetic response of ferrite nanoparticles. This effect of RE doping is useful for modification of certain aspects of the magnetic property of the ferrites as stated earlier. The luminescence property of RE ions has generated a lot of interest in recent times with chemically stable lanthanum (La) ions being photoluminescent [22]. As a result of its elevated refractive and low dispersive index values, this material finds relevance in manufacturing infrared (IR) absorbing glass and other industries like water treatment, biomedicine and electrode making amongst others [23, 24]. Variation in the values of magnetic saturation ( $M_s$ ), retentivity, coercivity and anisotropy has been reported as a result of presence of small amounts of RE in ferrite nanoparticles [25–27]. This impact of RE addition to ferrites makes them useful for magnetic recording applications [28] and high density storage of digital data [29]. With higher atomic size, induction of RE in the ferrite lattice also affects the surface area which thus varies with RE doping and the uncompensated spin density at the surface of the nanoparticles generates a field that impacts the spin structure of the entire cobalt ferrite [27, 30]. A systematic variation is expected when different amounts of RE are

sequentially introduced in the ferrite matrix and their impact on the magnetic characteristics of the pure material may be isotropic or anisotropic [31–33]. The extent of the impact is detrimental on the percentage of RE introduced in the ferrite system. There are many studies on doping of rare earth with ferrites have been in either nanoscale or bulk system [34, 35] focussed on low amounts of rare earth doping. The presence of additional phases with increasing doping levels are attributed to large radii of the substituted RE cations. Single domain transition from multi domain in magnetic property was observed by Nongjai et al. [36] in cobalt ferrite doped with 7.5% Indium. Anisotropic energies varied with varying doping concentration of Gallium (from  $x=0$  to  $x=0.8$ ) in cobalt ferrite as observed by Song et al. [37] attributed to changes in the exchange integral due to doping. It was also observed that gallium prefers placement at the tetrahedral site. Mariosi et al. [38] used sol gel method to synthesise lanthanum doped cobalt spinel nanoferrite,  $\text{CoFe}_{(2-x)}\text{La}_x\text{O}_4$  (range of doping from  $x=0.025$  to 0.1) to explore the applications for water purification with a decrease in crystallinity due to these small lanthanum quantities in the samples. A series of RE metals such as holmium and others in a fixed atomic ratio of 1% were doped to cobalt ferrite and their adsorption studies were conducted that were dependent on the physical and chemical changes brought up by these doping materials to the existing ferrite sample [39]. Our group previously did a comparative analysis [40] on the efficiency of doping of same quantities of two different REs – La and Gd in the ferrite matrix. With this paper, taking this further with increased lanthanum doping, our aim was to arrive at a point of high quantity doping till a solubility limit reached where the effect of doping creates a counter intuitive effect that defeats the very purpose of adding an external impurity (RE) to ferrite nanoparticle. The implications of doping with higher concentration of rare earth metals in cobalt ferrite despite many available studies [41–43] and its correspondence to the materials' magnetic characteristics and the exact effect on the magnetic features as a result of such high level of doping has still not been fully explored.

In this present work, we have used the soft chemical approach of microemulsion method. Our synthesis is aimed at making cobalt ferrite with high concentration of  $\text{La}^{3+}$  whilst controlling the presence of additional impurities. The low temperature gradual process of microemulsion is expected to provide time for integration of the substantial concentration of RE ion into the ferrite matrix to obtain highly pure integrated material. The proposed uniformity in morphology that is a characteristic of this methodology is another added advantage [41, 42]. We have focussed on the impact of high concentration of doping on the magnetic state of the ferrite material due to rare earth. In case of La, there has been no comprehensive study about the solubility limit of La within the cobalt ferrite matrix. As a result,

despite availability of various studies that are but limited to lower cationic substitution, the complete and exact magnetic picture is unclear. We have been able to synthesise nanoparticles with doping of high concentration of La to cobalt ferrite without the presence of additional impurities for  $x > 0.14$  with consequent decreasing coercivity and decreasing magnetic saturation. Additionally, we have been able to reduce hysteresis losses with doping at room temperature. To explore the complete magnetic picture as La is inserted into the ferrite lattice, and Mössbauer spectroscopy and SQUID magnetometry techniques have been utilised to explore the local and bulk magnetic properties, respectively. We have also studied the impact on characteristic optical response of cobalt ferrite nanoparticles due to La doping. The mechanism of changes in the magnetic as well as optical properties of the cobalt ferrite nanoparticles due to La doping have been examined.

## 2 Experimental

Microemulsion process was utilised for the synthesis of lanthanum doped cobalt ferrite. In the experimental method as reported [44], precursor solutions of iron (III) ( $\text{Fe}^{3+}$ ) and cobalt (II) ( $\text{Co}^{2+}$ ) cationic salts were mixed in with lanthanum (III) ( $\text{La}^{3+}$ ) nitrate in the ratio  $\text{Co}^{2+} : (\text{Fe}^{3+} + \text{La}^{3+})$  as 1:2 in double distilled water and were steadily added to a 50 mL sodium dodecyl sulphate (SDS)/n-hexane/butanol solution with continuous stirring till clear solution was achieved. This 1:2 ratio was achieved by adding lanthanum salt in  $x$  amounts and simultaneously decreasing corresponding amounts of ferric ions in the precursor solution by same  $x$  amounts with lanthanum concentration varying from  $x = 0.05$  to 0.15. A pure cobalt ferrite sample (CF) was also synthesised using the same procedure and reaction conditions for comparison purpose. To form stable microemulsion, an amount of SDS greater than the stoichiometric amount was used. After 20 h of continuous stirring, 1N NaOH was added in measured steps to the reaction mixture to regulate the pH to 10. The mixture was heated at 80 °C with 7 mL triethylamine added till slurry formation. After several times of washing with deionised water and ethyl alcohol, the mixture was kept for drying overnight at a temperature of 80 °C. After that, calcination at 500 °C for three hours was done. The synthesised samples were named LCF1, LCF2 and LCF3 with increasing lanthanum doping ( $x = 0.05, 0.10, 0.15$ , respectively) and CF designated for pure cobalt ferrite sample.

The d8 Advance diffractometer (Bruker, Germany) with 1.54 Å wavelength using a copper K- $\alpha$  source was used for recording XRD data. TEM images were captured on a microscope JEOL 2100. PL was done on a Horiba Jobin Yvon Fluoromax-4 spectrofluorometer. Magnetic measurements

were performed using a MMPS XL 7 SQUID magnetometer made by Quantum Design, USA, and Mössbauer spectroscopy was conducted using a gamma ray source as 10 mCi Co-57 in Rhodium matrix. Both SQUID and Mössbauer measurements were done at UGC-DAE CSR, Kolkata.

## 3 Results and discussion

From the XRD and TEM result analysis, many changes are observed in the structure due to doping. The obtained XRD peaks of cobalt ferrite doped with varying La amounts are compared with the JCPDS file #22–1086 which is the reference powder XRD pattern for pure cobalt ferrite. The XRD pattern of all the samples contain the most intense peak indexed at (311). The Rietveld refinement [45] of the diffraction pattern is done by the use of the MAUD software [46]. With increasing La concentration, the sharpness of the XRD pattern decreased and distortion is observed in the XRD pattern. The values extracted from the refinement performed such that of lattice parameters, crystallite size along different crystallographic directions and rms microstrains are presented in Table 1. The obtained values are evaluated against the experimental data. The fitting quality is evaluated by calculating various mathematical factors such as goodness of fitting (GoF) and the expected error ( $R_{\text{exp}}$ ) as well as the weighed residual error ( $R_{\text{wp}}$ ). The iteration of the parameters that was not halted till the convergence was reached and the goodness of fit value was found to lie in the range 1.73–2.33 for different samples, which represents a reasonably good fitting. According to the fault probability analysis treatment by Warren [47], planar defects of three kinds are to be used as refinable parameters. These are the two deformations, intrinsic ( $\alpha'$ ) and extrinsic ( $\alpha''$ ) and twin ( $\beta$ ) fault probabilities. The difference between intrinsic and extrinsic deformations is calculated from  $\alpha' - \alpha''$  and known as the deformation stacking fault probability. Table 1 contains the values of  $\alpha$  and all other parameters for all the samples.

As illustrated in Fig. 1, the diffraction pattern is presented for the cobalt ferrite and La doped cobalt ferrite as well as variation of lattice parameter, crystallite size and microstrain with variable doping amounts. The lattice constant shows lattice shrinkage for 5% doping concentration and increases thereafter with the concentration. Usually, the expansion or shrinkage in lattice depends upon the ionic size of the dopant. The ionic radii of  $\text{La}^{3+}$  (~0.103 nm) ions are much greater than the ionic radii of  $\text{Fe}^{3+}$  (~0.06 nm) ions. So, the lattice is expected to expand with doping concentration. On the contrary, the analysis shows shrinkage of lattice LCF 1 (i.e.at 5% doping concentration). This may be due to the lattice distortions as a result of La substitution causing fluctuations to the bond length and bond angles [48, 49]. The increment observed in lattice parameter for higher doping

**Table 1** Summarised x-ray diffraction data from experimental pattern and Rietveld analysis of sample CF, LCF 1, LCF 2 and LCF 3

Sample name	La doped Cobalt Ferrite / $\text{CoFe}_{2-x}\text{La}_x\text{O}_4$	From experimental parameters			From Rietveld analysis				G.O.F	
		Diffraction Angle ( $2\theta$ ) (degree)	Lattice constant, $a(\text{\AA})$	X-ray density, $(d_x)$ ( $\text{g}/\text{cm}^3$ )	Lattice Parameter, $a$ (nm)	Crystallite size, $(D_{\text{XRD}})$ (nm)	r.m.s strain, $<\epsilon_L^2 >^{1/2} \times 10^3$	Net deformation Probability ( $\alpha$ )		Twin fault probability, ( $\beta$ )
CF	$x=0.0$	35.8	8.29	5.34	0.8324	11.6 (220) 12.1 (311)	0.1	0.0031	–	2.33
LCF 1	$x=0.05$	35.8	8.3	5.54	0.8317	11.4 (511) 13.2 (220) 13.5 (311)	0.314	0.0038	3.08E-04	1.73
LCF 2	$x=0.10$	35.8	8.3	5.61	0.8339	13.1 (511) 15.7 (220) 17.6 (311)	1.56	0.0068	0.006	1.88
LCF 3	$x=0.15$	35.9	8.3	5.75	0.837	15.1 (511) 11.9 (220) 11.9 (311) 11.9 (511)	0.015	–	–	1.98

concentration obeys Vegard's law because the lattice has to accommodate for the higher ionic radii of lanthanum in place of smaller ferric ion vacancy. The crystallite size and microstrain increases with increasing doping concentration up to 10% i.e. up to LCF 2 as expected. However, both crystallite size and microstrain have decreased for LCF 3 (at 15% doping concentration) [50]. From reported results on RE doping [51, 52], it can be assumed that solubility limit of  $\text{La}^{3+}$  in the ferrite lattice is reached for LCF 3. The rearrangement of ferric and cobaltous ions amongst the octahedral and tetrahedral interstices to give more room to the RE ion increases the tendency of strain to the lattice. The shrinkage of the lattice parameter is the counter response to this increasing strain for relaxation as reported [53, 54]. Since the strain increases with doping, its shrinkage effect is more visible for higher  $x$  values. The analysis shows presence of defects in the crystal. The net deformation probability increases with the increase in doping concentration. Twin fault probability is found in low concentration of La doping in cobalt ferrite. However, no reasonable values of defects can be found at the highest concentration as can be inferred from measurements presented in Table 1. No peaks other than the parent material is observed, which suggests that the doped element ( $\text{La}^{3+}$ ) has either substituted the parent element ( $\text{Fe}^{3+}$ ) or has sat into the interstitial position of elemental lattice structural chain of the parent material. As no additional phase is confirmed, it can be assumed that the excess lanthanide ions are expected to sit at the grain boundaries and cause defect and impurities within the crystallite system. The growth of the crystallite is also affected as the energy is consumed in lattice expansion to accommodate lanthanum ions that increases lattice strain.

From the analysis of the TEM image as seen in Fig. 2 for the sample LCF 2, the average particle size is calculated,  $D_{\text{TEM}}$ . This size for doped ferrite samples is in the bracket of 13 to 16 nm and then decreases to 10 nm with increasing lanthanum doping as mentioned in Table 4. An affinity for cubical shape is also observed. This appreciation and then depreciation in size of the particle is due to addition of La with larger ionic radii as previously discussed from the results from Rietveld analysis. The size reduction with further rise in doping concentration is because of poorer crystallinity and reaching of solubility limit as has been discussed previously. Figures S1 and S2 are the TEM images for other doped samples available in the supplementary data. The deviation from spherical towards cubical shape can be explained in terms of a strong anisotropy. Also, along with usual forces, magnetic nanoparticles additionally experience magnetic interactions amongst their nanoclusters usually along the anisotropic axis. This causes non uniformity in particle shape. With addition of La to the cobalt ferrite lattice, these forces experience an increase in their magnitude because of which microstrain is increased. The combination

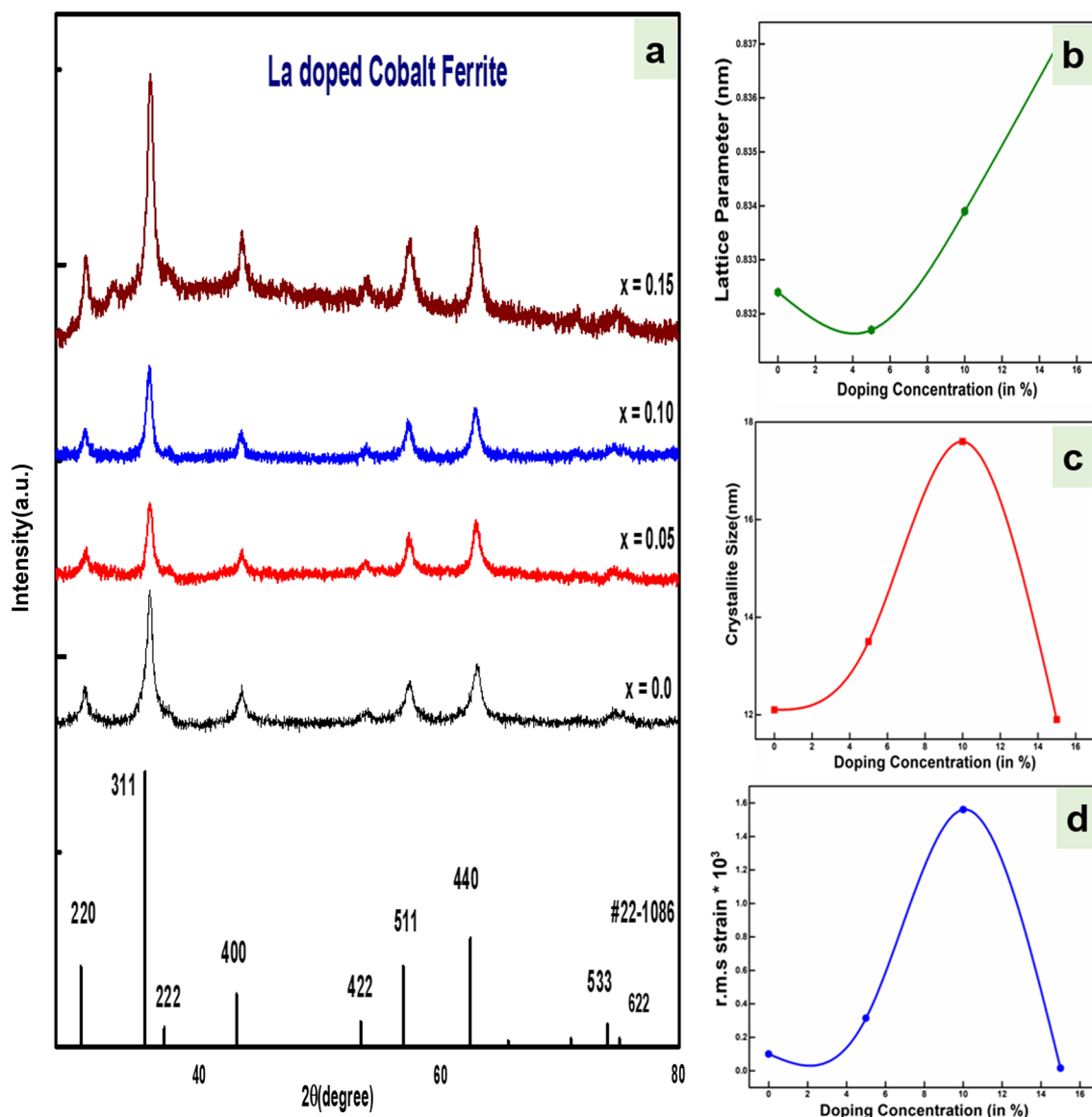


**Fig. 1** **a** XRD patterns for all the samples with doping concentration  $x=0, 0.05, 0.10, 0.15$  (samples CF, LCF 1, LCF 2 and LCF 3) along with JCPDS data # 22- 1086 of standard cobalt ferrite, **b** Variation

of lattice parameter with % of doping concentration, **c** crystallite size vs. doping concentration, **d** r.m.s strain vs. % doping concentration obtained from Rietveld analysis

of these causes increase in the agglomeration [28]. The d-spacing values from the SAED pattern also show deviation from the conventional values for nanocobalt ferrite. The main reason for this occurrence is the replacement of a smaller sized ion by a larger one (Fe in this case replaced by La) that has increased the micro strain on the lattice as a consequence. The particle size is determined using ImageJ software and the average particle diameter is calculated by the use of lognormal distribution function [55],

$$p(d) = \frac{1}{ds(2\pi)^{1/2}} \exp\left(-\frac{\ln^2(d_0/d)}{2s^2}\right) \quad (1)$$

where  $d$  and  $d_0$  are the particle size and the most probable size respectively with  $s$  as standard deviation. From HRTEM in the Fig. 2c, we can see the "magnetic dead layer (MDL)" at the boundary of the nanoparticle. The nanoscaling of any material leads to greater dependency on surface effects that dominate the resultant material properties in comparison to bulk. The magnetic properties of any material also follow from the same. The ordering of the surface particles critically contributes to the consequent magnetic characteristics. The enhanced frustration of the surface magnetic coupling leads to degradation of the ferromagnetic character in materials with highly magnetic in bulk form leading to formation of the magnetically dead layer at nanoscale [56]. The



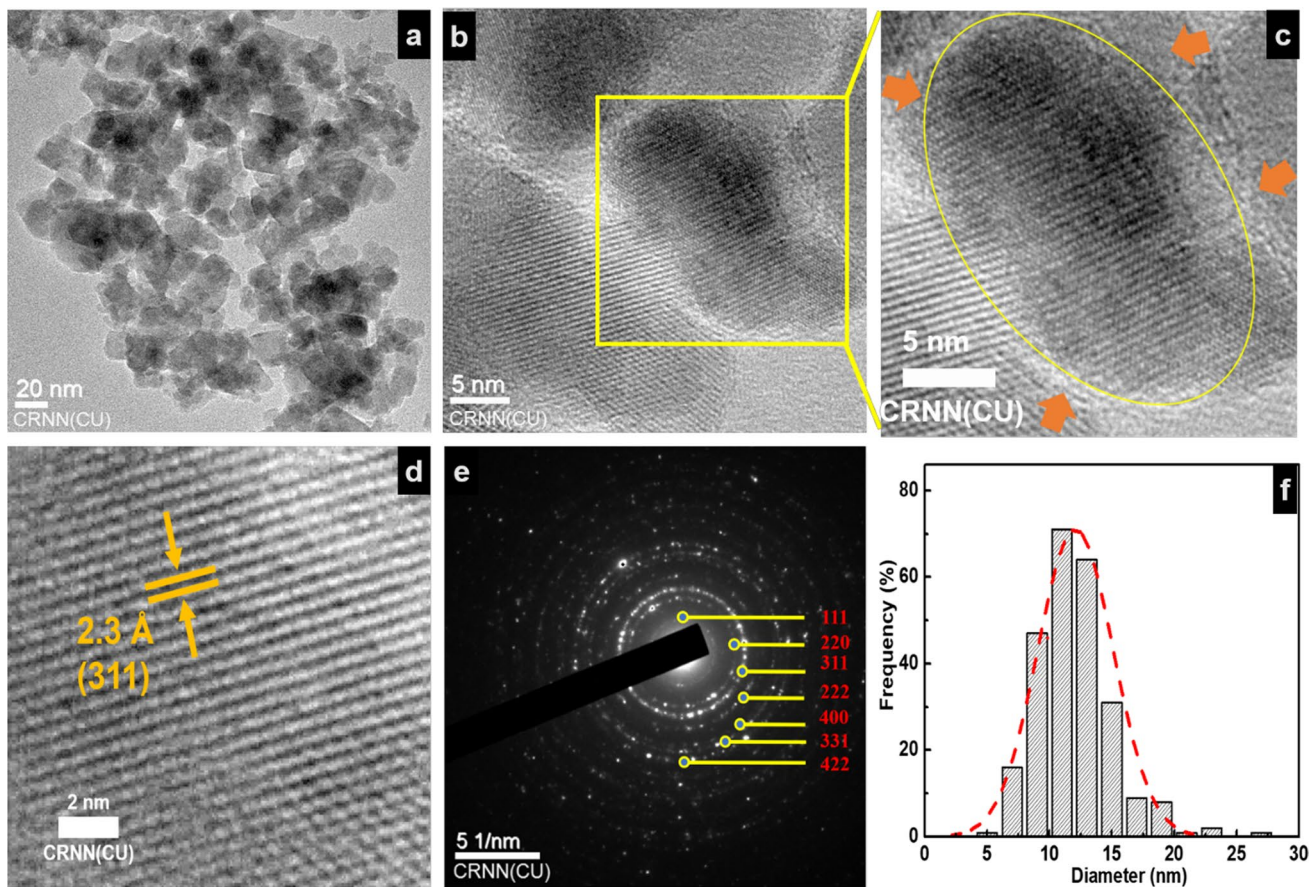


**Fig. 2** **a** TEM Micrograph for LCF2, **b** HRTEM micrograph, **c** HRTEM micrograph showing magnetic ‘dead layer’, **d** HRTEM micrograph showing d-spacing. **e** SAED pattern and **f** Lognormal distribution of nanoparticle size

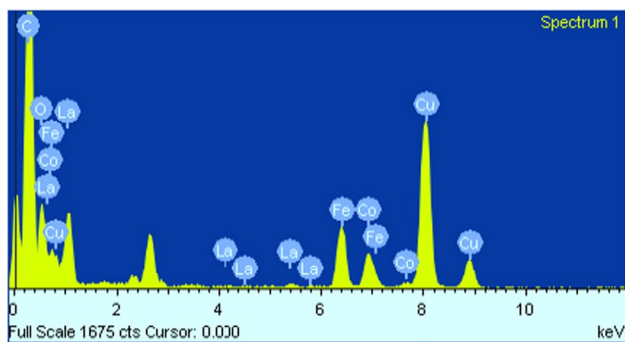


**Fig. 3** EDAX spectrum for LCF1/  $\text{CoFe}_{2-x}\text{La}_x\text{O}_4$  for  $x=0.05$

trigger for this here is the presence of lanthanum which has no magnetic moment at room temperature. The coupling of the other two cations is affected by the 3d-4f coupling introduced due to lanthanum leading to MDL [57, 58]. This is discussed in detail in the next section along with the magnetic data. The EDAX spectrum confirms the inclusion of La in the matrix of cobalt ferrite as shown by Fig. 3 and Table 2.

**Table 2** EDAX based composition of samples CF and LCF 1, LCF 2, LCF 3

$\text{CoFe}_{2-x}\text{La}_x\text{O}_4$  ( $x=0, 0.05, 0.10, 0.15$ )

Element	Atomic ratio with respect to cobalt			
	CF	LCF 1	LCF 2	LCF 3
Fe	2.31	1.96	1.89	1.83
Co	1	1	1	1
La	0	0.04	0.08	0.17

The iron composition in the cobalt ferrite decreased with increase in La doping in the matrix as intended.

### 3.1 Magnetic studies

Superconducting Quantum Interference Device (SQUID) magnetometer is operated at temperatures of 5 K and 300 K to measure the changes in magnetization (M) value with application of magnetic field (H) in the range from  $-5$  T to 5 T. Figure 4 shows the plotted hysteresis curves at both temperatures for the undoped cobalt ferrite and the La-doped

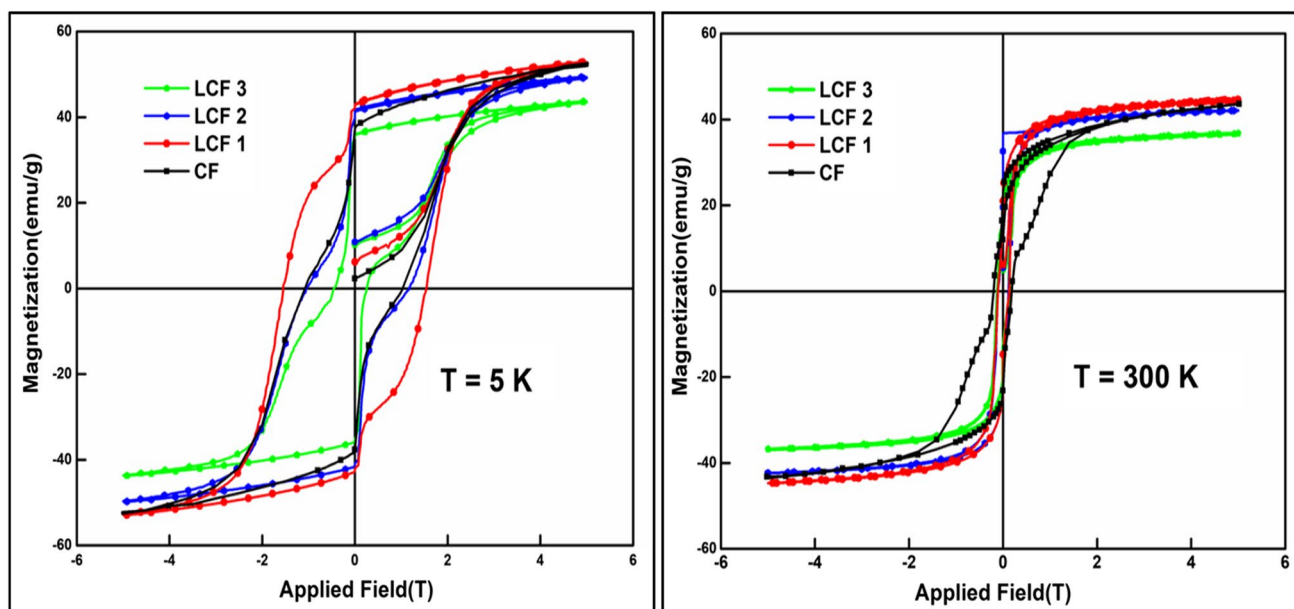


**Fig. 4** Magnetization v/s applied field at 5 and room temperature (RT) for pure and La doped cobalt ferrite samples. The  $M_s$  at 5 K is higher than the RT values (Table 3) due to decreasing thermal fluctuation effects on the magnetic particles at that (5 K) temperature

samples. It can be observed that the saturation is still not reached at this high field value despite demagnetisation prior to measurements.

The law of approach to saturation (LAS) [59] is used for anisotropy calculation by fitting the hysteresis curve to the it as per the Eq. (2),

$$M(H) = M_s \left( 1 - \frac{A}{H} - \frac{B}{H^2} \right) + \chi_n H \quad (2)$$

$$\text{where } B = \left( \frac{8}{105} \left( \frac{K_1}{\mu_0 M_s} \right)^2 \right)$$

The first term  $A/H$  is valid only for determinate range of applied magnetic field and is negligible at advanced fields and temperatures. The last term is a paramagnetic like term considered as a high-field magnetization resulting from an increase in spontaneous magnetization with the applied field, that can arise even from the sample itself [60]. The magnetization values corresponding to high applied magnetic field values are fitted to the LAS function are given by the Eq. 2 is illustrated in Fig. 5. Therefore, the spline fitting of  $M$  vs  $1/H^2$  at high field values is used to determine magnetic anisotropy ( $K_1$ ) values. Here,  $\mu_0$  is the permeability of free space. Table 3 consists of all summarised values of remanence ( $M_r$ ) and coercivity ( $H_c$ ), magnetisation of saturation ( $M_s$ ), squareness ratio ( $M_r/M_s$ ), and anisotropy constant ( $K_1$ ) for the samples CF and LCF 1–3 at the temperatures 5 K and 300 K. The coercivity and remanence values obtained at 5 K are found to be higher than those obtained at

room temperature. From the tabulated data, the subsequent decrease in value of magnetic saturation is observed with increase in doping that can be attributed to magnetically ‘dead’ surface layer. The localised 4f electrons in the rare earth (RE) ions lead to their magnetic moment and their magnetic ordering temperature is of the order of 40 K making them magnetically non-interacting ions in the lattice at room temperature leading to this dead layer which is more relevant in case of lanthanum that has zero magnetic moment because of absence of electron in its f-orbital [61]. The decrease in saturation magnetisation is also due to decreased sublattice interactions because of doping. The magnitude of Fe–La interaction, here, A–B interaction (B–octahedral site and A–Tetrahedral site), is less than that of Fe–Fe and Fe–Co interactions for pure cobalt ferrite. Since the A–B ionic interactions are major contributors to the magnetization of the material, therefore, the increase in La doping concentration decreases the number of Fe–Fe interactions and the magnetic saturation decreases. Due to doping, the equilibrium of A–A, B–B and A–B interactions that give a distinct magnetic character to cobalt ferrite is also disturbed [27, 62]. In a study by Khan *et al.* [63], doping cobalt ferrite with nickel (which is magnetic) produces a softer ferrite. Thus, the addition of non-magnetic  $\text{La}^{3+}$  and subsequent lowering of ionic concentration of  $\text{Fe}^{3+}$  has consequences on the magnetic properties of the ferrite sample which also vary with lanthanum amounts. The wasp-waisted 5 K hysteresis loop is due to existence of stable ferromagnetic (FM) and anti-ferromagnetic (AFM) ordering in the system. The cationic distribution and exchange interactions largely

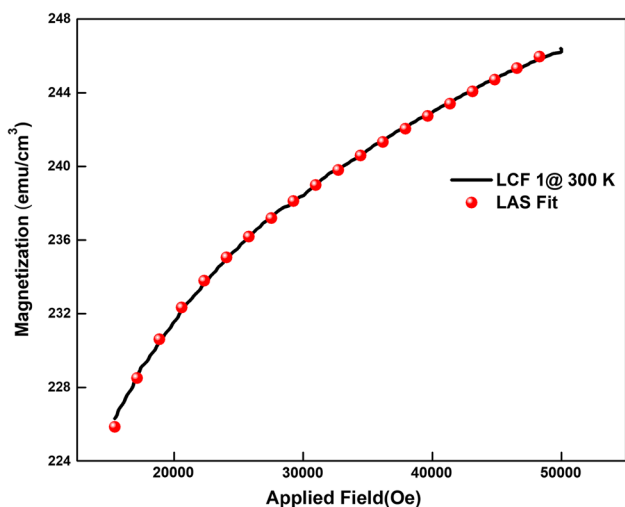


Fig. 5 LAS fit for sample LCF 1

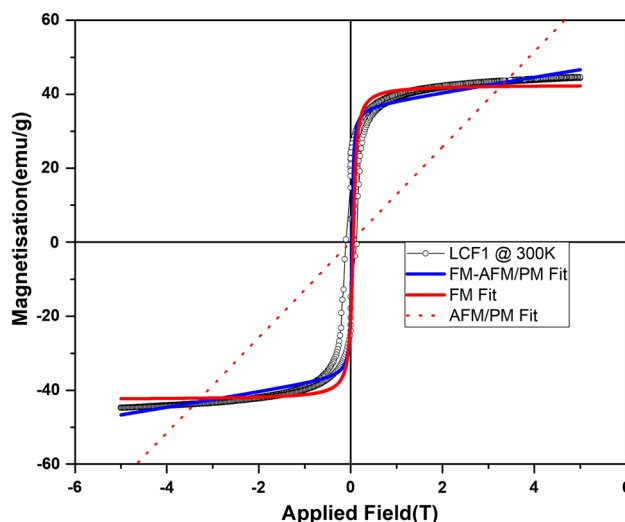


Fig. 6 M-H graph of LCF1 at 300 K and fitted with Eq. (3)

influence the magnetic properties of the mixed spinel cobalt ferrite. Such mixed spinels contain both mixed interactions i.e. super-exchange ( $\text{Fe}^{3+}\text{-O}^{2-}\text{-Fe}^{3+}$ ) and double – exchange ( $\text{Co}^{2+}/\text{Fe}^{2+}\text{-O}^{2-}\text{-Fe}^{3+}$ ) occurring at room temperatures and below as reported [64]. This leads to simultaneous presence of FM and AFM phases that compete.

With the intention to understand and determine the type of magnetic interactions and the contribution of FM and AFM parts with doping, M-H values were fitted according to the equation [65]:

$$M(H) = \left[ 2 \frac{M_{SFM}^2}{\pi} \tan^{-1} \left\{ \left( \frac{H \pm H_{ci}}{H_{ci}} \right) \tan \left( \frac{\pi M_{RFM}}{2M_{SFM}} \right) \right\} \right] + \chi H \tag{3}$$

where  $M_{SFM}$  is FM saturation magnetisation,  $M_{RFM}$  is remanent magnetisation,  $H_{ci}$  is intrinsic coercivity and  $\chi$  is the magnetic susceptibility observed for the anti-ferro / para-magnetic part. As can be seen in Fig. 6, the first part of the equation represents the contribution due to FM part and the second part is due to the linear contribution from the AFM/PM part. It is found that the values of these parameters are lower for undoped sample compared to the doped samples and increases monotonically with increasing doping as

reported elsewhere [66, 67] due to anisotropy and increase in coupling exchange. This also increases the remanence ratio.

In the matrix of an inverse spinel like cobalt ferrite, the trivalent RE cation (La) can only occupy the octahedral site because of its large atomic radius. This impacts the occupancy of cobaltous ions present there that are forced to migrate to tetrahedral site. The changed occupancy misbalances the spin alignments which are covered in detail in the Mössbauer spectroscopy results in the next section.

Between temperatures 5 K to 300 K, the field-cooled (FC) and zero field-cooled (ZFC) measurements are taken at the applied external magnetic field of 100 Oe and the magnetic moment,  $m$  (emu/g) v/s temperature,  $T$  (K) curves are plotted for all the samples as seen in Fig. 7a, b. The curve is considered in two parts where the upper section represents the moment values in FC state whilst the lower portion represents the moment values obtained in ZFC state.

As seen in Fig. 7a, in FC measurement, the cooling of the sample is done from room temperature (300 K) to the lowermost temperature (here, 5 K) in presence of magnetic field and magnetic moment is recorded in the heating cycle. In theory, at the lowest temperature, nearly all the magnetic moments are ordered, and a maximum is obtained. The

Table 3 Summarised SQUID measurements

Sample	La doped Cobalt Ferrite ( $\text{CoFe}_{2-x}\text{La}_x\text{O}_4$ )							
	x = 0/CF		x = 0.05/LCF 1		x = 0.10/LCF 2		x = 0.15/LCF 3	
Temperature	5 K	300 K	5 K	300 K	5 K	300 K	5 K	300 K
$M_r$ (emu/g)	37.26	6.02	42.76	23.93	41.3	21.7	35.82	20.78
$H_c$ (T)	1.08	0.02	1.55	0.11	1.2	0.1	0.45	0.12
$M_s$ (emu/g)	80.05	52.7	55.05	45.5	49.3	42.1	47.2	36.81
$M_r/M_s$	0.47	0.11	0.78	0.53	0.84	0.67	0.76	0.56
$K_1$ ( $\times 10^5 \text{ J/m}^3$ )	13.9	2.65	16.7	2.83	17.3	2.94	14.2	2.77



sample is then gradually heated that causes fluctuations due to increasing thermal energy and magnetization value steadily decreases.

During ZFC measurements, the sample cooling is executed in absence of magnetic field, moments of relaxing particles are not ordered but at lowest temperature moments freeze (known as blocked state) with moments oriented randomly giving a low magnetization value. As the sample is heated, it gains thermal energy that causes some moments to align giving an upward trend in magnetization value. This continues till a temperature is reached known as the blocking temperature when moments start flipping coherently causing superparamagnetic relaxation. Accordingly, blocking temperature is assessed from highest extremum of the ZFC curve. Beyond that temperature magnetisation starts falling as seen in Fig. 7(b) and at a higher temperature magnetization value merges with that of the FC magnetization value. This is known as the temperature of irreversibility,  $T_{irr}$ , which does not depend on doping concentration. Blocking temperature certainly depends on La doping concentration. The temperature of blocking of the CF sample is about the order of 300 K as its  $T_B$  and  $T_{irr}$  seem to coincide. However, in case of La doped samples, values are about 45 K, 38 K and 36 K for samples LCF 1–3, respectively in order of increasing doping. This decrease coincides with reduction in particle size and rise in anisotropy [21, 61].

The particle sizes calculated from XRD, TEM and SQUID analyses are compared in Table 4, and it is found that  $D_{XRD} > D_{TEM} > D_m$  where  $D_m$  is the SQUID calculated size or the critical size of particle for single domain. This is in accordance with several reported results where  $D_m$  calculated is found considerably lower than the particle size calculated otherwise [59].

### 3.2 Photoluminescence

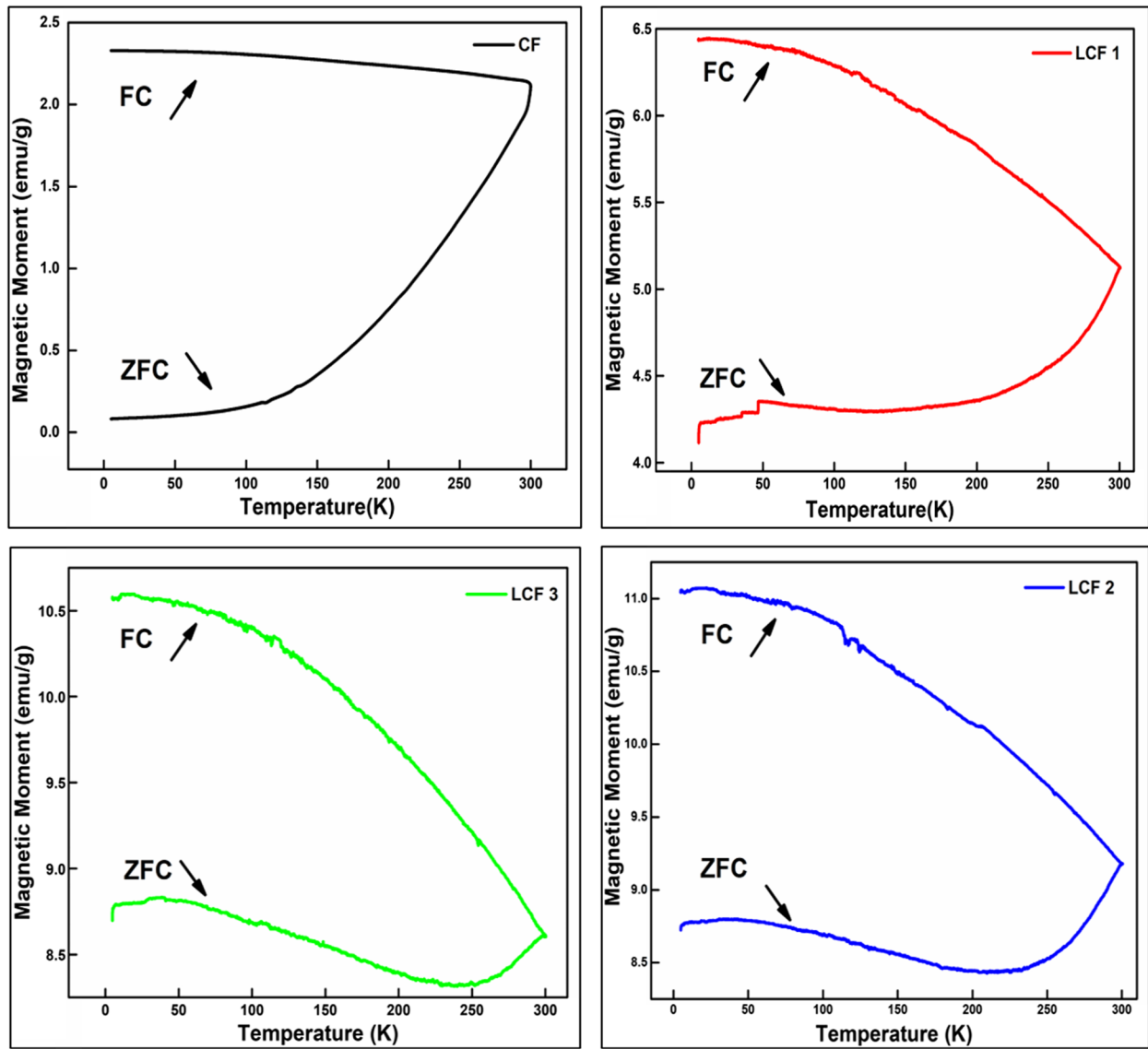
PL spectroscopy is a non-contact and non-destructive characterisation method that gives information regarding the electronic states and the transitions amongst them on application of light radiation on the material. The photoexcitation or absorption of photon as a result causes the electronic excitation to jump to a higher electronic state of the material. When the electron returns to its ground state, a photon is emitted. This emitted light gives information about electronic arrangement inside the material. In this case, we are interested in determining the state of electronic transitions due to presence of lanthanum in cobalt ferrite. Conventionally, in ferrites, electrons responsible for PL spectra are present in the conduction band and some temporary localised trap states created near the conduction band due to lattice defects and surface effects as a result of quantum confinement [68, 69]. Here, as we purposefully created defects by doping La, the intensity first increased and then decreased

as can be seen in Fig. 8. These transitions are schematically represented in Fig. 9. Here, the two prominent transitions are at 413 nm and 433 nm. The transition at 413 nm corresponds to near band edge transition (NBE) as reported [70] due to the recombination of excited electron hole pair just below the conduction band and valence band. The cationic exchange occurring inside the material to accommodate La causes formation of shallow donor levels. Instead of transition to occur between  $E_c$  and  $E_v$ , it occurs between an energy level below  $E_c$  and  $E_v$  at wavelength of 434 nm emitting violet light. Other transitions such as of the order of 460 nm and above are a result of defects created by cationic migration of ferric ions and redistribution of cobaltous ions between octahedral and tetrahedral sites. This ionic migration can be corroborated from the results from Mössbauer spectroscopy. The broad emission spectra hence can be the effect of creation of these direct and indirect band gaps due to the transitions between these shallow energy levels [71]. The broadened peaks at higher wavelengths is also due to oxygen vacancies where electron–hole recombination occurs [72, 73]. The luminescence of the ferrite material is enhanced with La doping compared to the undoped sample. However, the decrease in PL intensity with increase in La concentration from LCF1 to LCF3 can be attributed to stoichiometric decrease in  $Fe^{3+}$  which perhaps decreases the mobility of the charge carriers and is seen leading to concentration quenching with increase in La/Fe ratio [54, 55]. Higher La concentration, due to the poor crystalline quality as described by the Rietveld data analysis, causes defects that impacts the distribution of excited electrons between various transitions. As a result, the intensity is greatly reduced for higher  $x$  value ( $x = 0.15$ ) i.e. LCF3 compared to other samples. Also, due to this reason, multiple electronic transitions occur [70, 76]. When we compare relative intensities of the doped samples, the decrease in size of particles is not significant to impact the PL. The particle size in doped samples LCF 1–3 is comparable that of the pure sample CF which has a smaller particle size which results in decreased PL intensity for CF as reported [77].

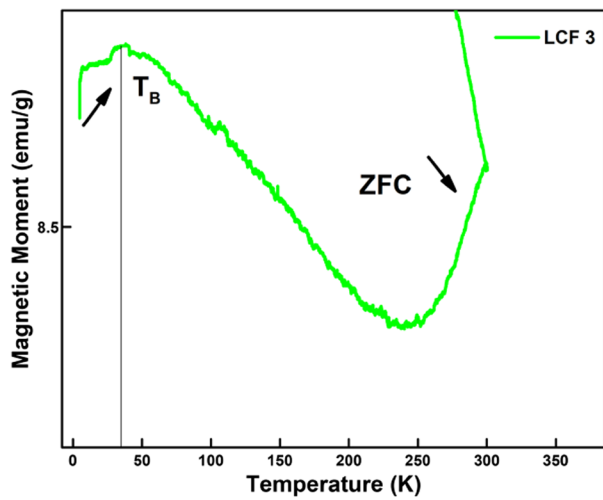
### 3.3 Mössbauer spectroscopy

Mössbauer spectroscopy conducted at 300 K by means of a 10 mCi Co-57 as the source of  $\gamma$ - rays in Rh matrix is utilised in determination of parameters such as hyperfine field ( $H_{int}$ ), quadrupole splitting (Q.S) and isomer shift (I.S) to gain information regarding the local environment and valence state of iron atoms in the given crystal lattice and the nature of magnetic ordering. Being a local probe, it gives accurate insight on the changes of local environment around the iron atoms of the crystal.

From Fig. 10 it is clear that Mössbauer spectra of the CF sample as well as the La –doped samples consist of a



(a)



(b)

**Fig. 7** **a** FC-ZFC at external magnetic field of 100 Oe for undoped and La doped cobalt ferrite. **b** ZFC at 100 Oe applied magnetic field for La doped cobalt ferrite sample LCF 3

**Table 4** Comparison of particle sizes from XRD, TEM and SQUID

Sample	La doped Cobalt Ferrite/ $\text{CoFe}_{2-x}\text{La}_x\text{O}_4$	$D_{\text{XRD}}$ (nm)	$D_{\text{TEM}}$ (nm)	$D_m$ (nm)
CF	$x=0.0$	12.5	12.1	7.21
LCF 1	$x=0.05$	14.3	13.6	7.25
LCF 2	$x=0.10$	15.8	15.7	7.22
LCF 3	$x=0.15$	11.4	10.3	7.18

predominate sextet with broad lines along with a central doublet. The sextet patterns imply the blocked state of these nanoparticles at this temperature. All Mössbauer spectra were fitted with two sextets and a doublet. The hyperfine parameters obtained from the fitted spectra are shown in Table 5. The two fitted sextets are assigned to the B & A (octahedral & tetrahedral respectively) sites of the ferrite structure. The central doublets are assigned to finer ferrite particles in these samples undergoing superparamagnetic relaxation [78].

The hyperfine parameters evaluated for all samples as given in Table 5 are different for the two sextets due to different coordination number of trivalent iron ions for A and B sites. Considering the 2 sextets in all spectra, the one with the lesser isomeric shift value is usually designated for the tetrahedral site. This is because of lower covalency and larger Fe–O bond separation at octahedral sites that instigates higher isomeric shift (I.S.) at this site [79]. The I.S. values do not vary significantly with doping. So it can be concluded that the density of s-electronic cloud is mostly unaffected by presence of lanthanum in the matrix [80, 81]. However, a close inspection of tabulated data (Table 5) reveals a few interesting aspects. It is seen that quadrupole splitting (QS) of octahedral sites increased due to La-doping but QS of tetrahedral sites did not get affected. This indicates that doped La ions mainly replace Fe atoms in octahedral sites causing alteration of electric field gradient (EFG) around the Fe nuclei. The electric field asymmetry surrounding the Mössbauer nucleus is caused by changes to the cubic symmetry which is in good agreement with the variation in rms strain values calculated from the Rietveld analysis as discussed and causes changes in Q.S values [82–85]. Evidence of La inclusion in the octahedral sites is also clear as  $H_{\text{int}}$  of the octahedral site is less in the LCF samples compared to that in the CF sample. Presence of paramagnetic La in the place of Fe reduces the A-B interactions occurring between  $\text{Fe}^{3+}$ - $\text{Co}^{2+}$

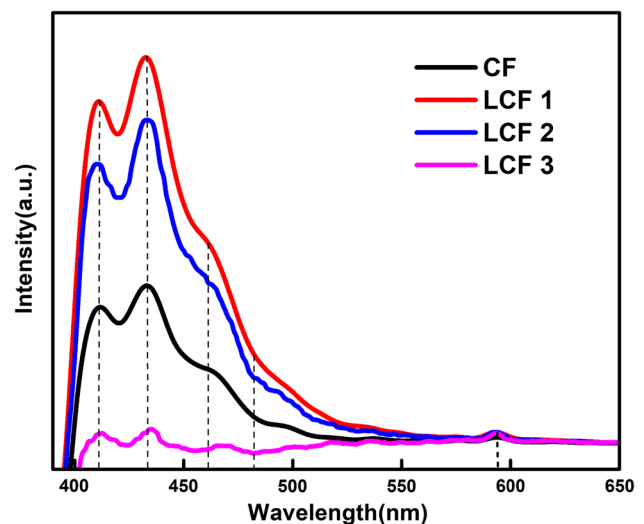


**Fig. 8** PL spectra of samples CF, LCF1, LCF2 and LCF3

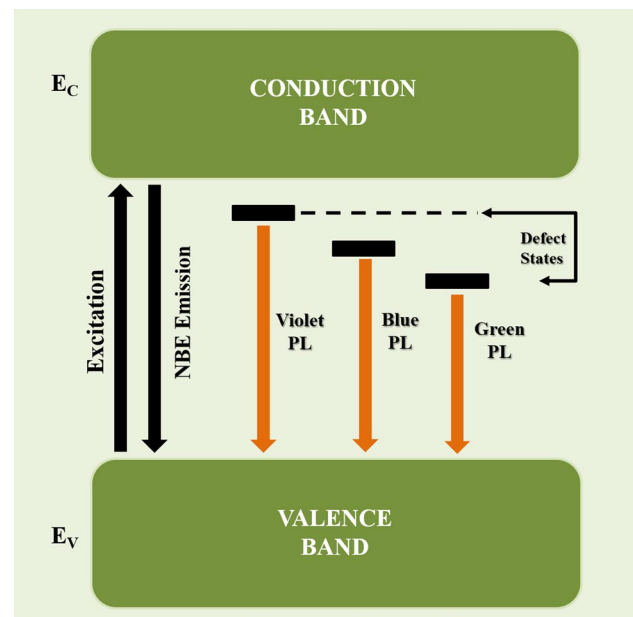


**Fig. 9** Energy band diagram illustrating proposed transitions due to defects

in the octahedral site and hence  $H_{\text{int}}$  reduces [86–88]. In fact,  $H_{\text{int}}$  for the octahedral site only shows reduction due to La doping. The tetrahedral site shows a reverse trend. This could be due the fact the displaced Fe atom from the octahedral site enters in the tetrahedral site and causes a complex Fe-Co-Fe interaction which enhances  $H_{\text{int}}$ . Cobalt Ferrite is an inverse spinel. The inversion parameter calculated as

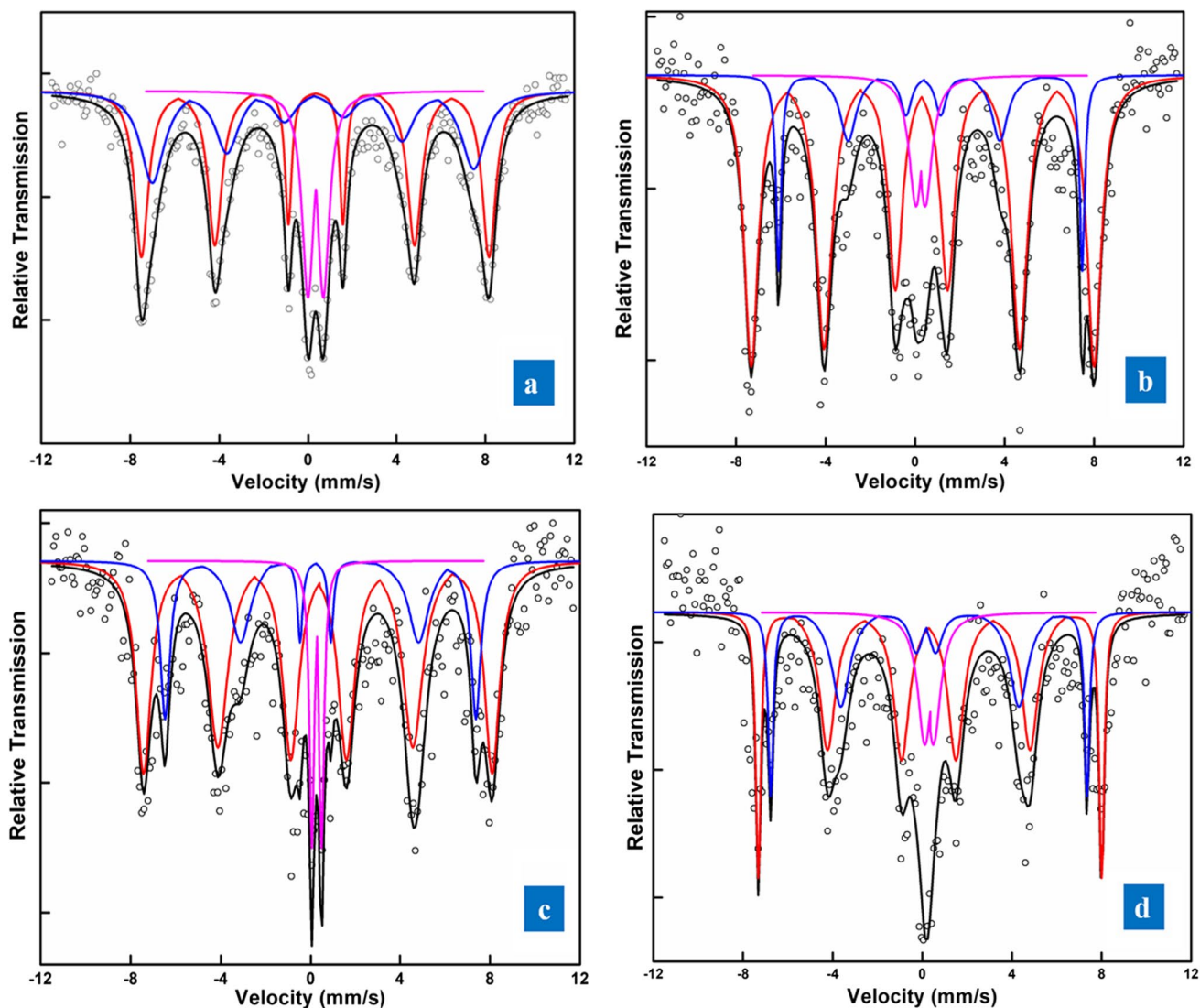


Fig. 10 a–d Mossbauer patterns for CF, LCF1, LCF2 and LCF3, respectively

$$\frac{I_B * 0.94}{I_A} = \frac{\lambda}{1 - \lambda} \quad (4)$$

is estimated to be 80% for the undoped sample that decreases with increase of doping concentration [89]. This indicates changes in cationic occupancy due to doping [27, 86].

## 4 Conclusions

The core characteristics of the cobalt ferrite material are significantly modified with high concentration doping of non-ferromagnetic La with larger radii and 4f electrons as valence electrons, which have been successfully integrated

into the ferrite matrix by the microemulsion method. This is also supported by the study of the features obtained from the Rietveld refinement of the diffraction data, which show significant structural deviation with the introduction of La with increase in crystallite size up to a certain doping percentage. The size variation is backed by size calculation from TEM. The magnetic data agrees with the domain size showing similar trend. The anisotropy is decreased with increased doping since the magnetism of the material is influenced. With the introduction of ferrimagnetic-antiferromagnetic coupling in the sample due to La doping, it has potential for multiferroic applications of the material [90–92]. The cationic reordering because of doping is evident from the results of the Mössbauer spectroscopy which show variations in values of quadrupole splitting and  $H_{int}$  in lanthanum doped samples. When looked in cognizance with the data



**Table 5** Mössbauer parameters for samples CF and LCF 1, LCF 2 and LCF 3

Mössbauer spectroscopy DATA					
For La substituted Cobalt Ferrite (CoFe <sub>2-x</sub> La <sub>x</sub> O <sub>4</sub> )					
	Sample Name	x=0 / CF	x=0.05 / LCF 1	x=0.10/ LCF 2	x=0.15/ LCF 3
Sextet 1 (Tetrahedral site)	I.S. (mm/s)	0.26	0.31	0.3	0.31
	Q.S. (mm/s)	0.06	0.04	0.11	0.06
	L.W.* (mm/s)	1.28	0.81	0.93	0.66
	H <sub>int</sub> (kOe)	450	476	482	476
	% Area	34.2	73.2	67.3	53.5
Sextet 2 (Octahedral Site)	I.S. (mm/s)	0.33	0.48	0.5	0.56
	Q.S. (mm/s)	0.02	0.29	0.4	0.5
	L.W. (mm/s)	0.62	0.57	0.62	0.65
	H <sub>int</sub> (kOe)	486	421	430	438
	% Area	44.9	15.5	23.2	28.7
Doublet	I.S. (mm/s)	–	0.25	0.26	0.3
	Q.S. (mm/s)	–	0.41	0.43	0.37
	L.W. (mm/s)	–	0.75	0.67	0.79
	% Area	–	11.3	9.5	17.8

\*Line width

from PL, there is occurrence of multiple peaks due to this rearrangement leading to modulation of electronic states of the two original cations. Also, enhanced optical activity at certain amount of La doping in cobalt ferrite is observed but showed a diminishing trend at higher concentration. This shows that the overall performance of this material depends on maintaining an optimal La/Fe ratio for effective application of this nanomaterial. For the doping above the solubility point, the impurity phase shows up separately, as inferred from the characterisation results. The possibility of modifying and enhancing magneto-optical properties by La doping becomes an interesting possibly in these materials.

**Supplementary Information** The online version contains supplementary material available at <https://doi.org/10.1007/s00339-023-07209-5>.

**Acknowledgements** The authors would like to recognize UGC-DAE CSR, Kolkata for facilitating Mössbauer spectroscopy and SQUID magnetometer equipments and the University of Calcutta operated CRNN for providing TEM facility. Prof. Anindya Datta is thankful to GGSIP University, New Delhi for the following FRGS grants: GGSIPU/DRC/FRGS/2018/1/ (1115) and GGSIPU/DRC/FRGS/2020/1988/6 and DST for FIST grant (SR/FST/PSI-167/2011(C)). The author (MG) is grateful to UGC for the fellowship.

**Author contributions** All authors contributed to the study. Anindya Datta and Satyabrata Mohapatra conceived and designed the experiments. The sample preparation, collection and analysis were conducted by Meenal Gupta. Rietveld Analysis of the XRD data was done by Saurav Datta and Meenal. Mössbauer data analysis was done by Dipankar Das and Anusree Das. The first draft of the manuscript was written by Meenal Gupta and all authors read and edited subsequent versions and approved the final manuscript.

**Data availability** All the information supporting the conclusions of doping of cobalt ferrite with lanthanum rare earth metal are available within the paper and the supplementary information files.

## Declarations

**Conflict of interest** There is no conflict of interest regarding the publication of this paper. Prof. Anindya Datta is thankful to GGSIP University, New Delhi for the following FRGS grants: GGSIPU/DRC/FRGS/2018/1/ (1115) and GGSIPU/DRC/FRGS/2020/1988/6 and DST for FIST grant (SR/FST/PSI-167/2011(C)). The author (Meenal Gupta) is grateful to UGC for the fellowship. No competing financial interests or relationships of personal stature are there that can influence the outcomes of the reported work.

## References

1. A.H. Lu, E.L. Salabas, F. Schüth, *Angew. Chemie - Int. Ed.* **46**, 1222 (2007)
2. T.E. Quickel, V.H. Le, T. Brezesinski, S.H. Tolbert, *Nano Lett.* **10**, 2982 (2010)
3. K.K. Senapati, C. Borgohain, P. Phukan, *J. Mol. Catal. A Chem.* **339**, 24 (2011)
4. C. Upadhyay, D. Mishra, H.C. Verma, S. Anand, R.P. Das, *J. Magn. Magn. Mater.* **260**, 188 (2003)
5. D.S. Mathew, R.S. Juang, *Chem. Eng. J.* **129**, 51 (2007)
6. M. Abbas, B. Parvatheeswara Rao, M. Nazrul Islam, K. W. Kim, S. M. Naga, M. Takahashi, and C. Kim, *Ceram. Int.* **40**, 3269 (2014).
7. T. Bala, C.R. Sankar, M. Baidakova, V. Osipov, T. Enoki, P.A. Joy, B.L.V. Prasad, M. Sastry, *Langmuir* **21**, 10638 (2005)

8. S. Ayyappan, J. Philip, B. Raj, *Mater. Chem. Phys.* **115**, 712 (2009)
9. P.C.R. Varma, R.S. Manna, D. Banerjee, M.R. Varma, K.G. Suresh, A.K. Nigam, *J. Alloys Compd.* **453**, 298 (2008)
10. N. Moumen, P. Veillet, M.P. Pileni, *J. Magn. Magn. Mater.* **149**, 67 (1995)
11. P.C. Morais, V.K. Garg, A.C. Oliveira, L.P. Silva, R.B. Azevedo, A.M.L. Silva, E.C.D. Lima, *J. Magn. Magn. Mater.* **225**, 37 (2001)
12. Q. Song, Z.J. Zhang, *J. Am. Chem. Soc.* **126**, 6164 (2004)
13. G. Baldi, D. Bonacchi, C. Innocenti, G. Lorenzi, C. Sangregorio, *J. Magn. Magn. Mater.* **311**, 10 (2007)
14. C. V. Gopal Reddy, S. V. Manorama, and V. J. Rao, *J. Mater. Sci. Lett.* **19**, 774 (2000).
15. I. Sharifi, H. Shokrollahi, S. Amiri, *J. Magn. Magn. Mater.* **324**, 903 (2012)
16. C. Upadhyay, H.C. Verma, S. Anand, *J. Appl. Phys.* **95**, 5746 (2004)
17. G.A. Sawatzky, F. Van Der Woude, A.H. Morrish, *J. Appl. Phys.* **39**, 1204 (1968)
18. J.P. Singh, H. Kumar, R.C. Srivastava, A. Singhal, N. Sarin, K.H. Chae, *Appl. Sci. Lett.* **2**, 3 (2016)
19. K.H.J. Buschow, *Reports. Prog. Phys.* **54**, 1123 (1991)
20. C.W. Nan, M. Li, X. Feng, S. Yu, *Appl. Phys. Lett.* **78**, 2527 (2001)
21. P. Roy, S. M. Hoque, S. I. Liba, and S. Choudhury, *AIP Adv.* **8**, (2018).
22. C. K. Jørgensen and R. Reisfeld, *New Trends Chem.* 127 (2008).
23. G. Blasse, B. C. Grabmaier, G. Blasse, and B. C. Grabmaier, *Lumin. Mater. I* (1994).
24. P. Mohn, *Magnetism in the Solid State* (Springer-Verlag, Berlin/Heidelberg, 2006)
25. N. Rezlescu, E. Rezlescu, C. Pasnicu, M.L. Craus, *J. Phys. Condens. Matter* **6**, 5707 (1994)
26. X. Liu, P. Hernández-Gómez, K. Huang, S. Zhou, Y. Wang, X. Cai, H. Sun, B. Ma, *J. Magn. Magn. Mater.* **305**, 524 (2006)
27. L. Zhao, H. Yang, X. Zhao, L. Yu, Y. Cui, S. Feng, *Mater. Lett.* **60**, 1 (2006)
28. A.K. Nikumbh, R.A. Pawar, D.V. Nighot, G.S. Gugale, M.D. Sangale, M.B. Khanvilkar, A.V. Nagawade, *J. Magn. Magn. Mater.* **355**, 201 (2014)
29. A.A. Kadam, S.S. Shinde, S.P. Yadav, P.S. Patil, K.Y. Rajpure, *J. Magn. Magn. Mater.* **329**, 59 (2013)
30. X. Meng, H. Li, J. Chen, L. Mei, K. Wang, X. Li, *J. Magn. Magn. Mater.* **321**, 1155 (2009)
31. L. Ben Tahar, M. Artus, S. Ammar, L. S. Smiri, F. Herbst, M. J. Vaulay, V. Richard, J. M. Grenèche, F. Villain, and F. Fiévet, *J. Magn. Magn. Mater.* **320**, 3242 (2008).
32. E. Ateia, M.A. Ahmed, A.K. El-Aziz, *J. Magn. Magn. Mater.* **311**, 545 (2007)
33. J. Song, L. Wang, N. Xu, Q. Zhang, *J. Rare Earths* **28**, 451 (2010)
34. I. Haïk Dunn, S. E. Jacobo, and P. G. Bercoff, *J. Alloys Compd.* **691**, 130 (2017).
35. G. Bulai, L. Diamandescu, I. Dumitru, S. Gurlui, M. Feder, O.F. Caltun, *J. Magn. Magn. Mater.* **390**, 123 (2015)
36. R. Nongjai, S. Khan, K. Asokan, H. Ahmed, and I. Khan, *J. Appl. Phys.* **112**, (2012).
37. S.H. Song, C.C.H. Lo, S.J. Lee, S.T. Aldini, J.E. Snyder, D.C. Jiles, *J. Appl. Phys.* **101**, 99 (2007)
38. F. R. Mariosi, J. Venturini, A. da Cas Viegas, and C. P. Bergmann, *Ceram. Int.* **46**, 2772 (2020).
39. X. Wu, Z. Ding, N. Song, L. Li, W. Wang, *Ceram. Int.* **42**, 4246 (2016)
40. M. Gupta, A. Das, D. Das, S. Mohapatra, A. Datta, *J. Nanosci. Nanotechnol.* **20**, 5239 (2020)
41. X. C. Zhong, X. J. Guo, S. Y. Zou, H. Y. Yu, Z. W. Liu, Y. F. Zhang, and K. X. Wang, *AIP Adv.* **8**, (2018).
42. Y. Zheng, G. Hussain, S. Li, S. Batool, and X. Wang, *Nanomaterials* **12**, (2022).
43. K.V. Zipare, S.S. Bandgar, G.S. Shahane, *J. Rare Earths* **36**, 86 (2018)
44. M. Gupta, A. Das, S. Mohapatra, D. Das, A. Datta, *Appl. Phys. A* **126**, 1 (2020)
45. H.M. Rietveld, *J. Appl. Crystallogr.* **2**, 65 (1969)
46. L. Lutterotti, (2002).
47. B. E. Warren, *X-Ray Diffr.* 381 (1990).
48. F. Ben Jemaa, S. Mahmood, M. Ellouze, E. K. Hlil, and F. Halouani, *J. Mater. Sci.* **50**, 620 (2015).
49. F. Ben Jemaa, S. H. Mahmood, M. Ellouze, E. K. Hlil, and F. Halouani, *J. Mater. Sci. Mater. Electron.* **26**, 5381 (2015).
50. M. Bedir, A. Tunç, M. Öztas, *Acta Phys. Pol. A* **129**, 1159 (2016)
51. E.E. Sileo, S.E. Jacobo, *Phys. B Condens. Matter* **354**, 241 (2004)
52. P.K. Roy, J. Bera, *Mater. Res. Bull.* **42**, 77 (2007)
53. L. Kumar, M. Kar, *Ceram. Int.* **38**, 4771 (2012)
54. M. Yehia, S.M. Ismail, A. Hashhash, *J. Supercond. Nov. Magn. Supercond. Nov. Magn.* **27**, 771 (2014)
55. R. W. Chantrell, J. Popplewell, and S. W. Charles, *Phys. B+C* **86–88**, 1421 (1977).
56. J. Curiale, M. Granada, H.E. Troiani, R.D. Sánchez, A.G. Leyva, P. Levy, K. Samwer, *Appl. Phys. Lett.* **95**, 10 (2009)
57. K. Tanbir, M.P. Ghosh, R.K. Singh, M. Kar, S. Mukherjee, *J. Mater. Sci. Mater. Electron.* **31**, 435 (2020)
58. M. P. Ghosh, S. Mandal, and S. Mukherjee, *Eur. Phys. J. Plus* **135**, (2020).
59. S. Chakrabarty, A. Dutta, M. Pal, *J. Magn. Magn. Mater.* **461**, 69 (2018)
60. H. Zhang, D. Zeng, Z. Liu, *J. Magn. Magn. Mater.* **322**, 2375 (2010)
61. L.D. Tung, V. Kolesnichenko, D. Caruntu, N.H. Chou, C.J. O'Connor, L. Spinu, *J. Appl. Phys.* **93**, 7486 (2003)
62. M.L. Kahn, Z.J. Zhang, *Appl. Phys. Lett.* **78**, 3651 (2001)
63. K. Maaz, S. Karim, A. Mashiatullah, J. Liu, M.D. Hou, Y.M. Sun, J.L. Duan, H.J. Yao, D. Mo, Y.F. Chen, *Phys. B Condens. Matter* **404**, 3947 (2009)
64. Atta Ur Rahman, M. A. Rafiq, K. Maaz, S. Karim, K. Hayat, and M. M. Hasan, *J. Nanoparticle Res.* **16**, 1 (2014).
65. S.R. Mohapatra, A. Swain, C.S. Yadav, S.D. Kaushik, A.K. Singh, *RSC Adv.* **6**, 112282 (2016)
66. K.L. Routray, D. Behera, *J. Mater. Sci. Mater. Electron.* **29**, 14248 (2018)
67. S. Chakrabarty, A. Dutta, M. Pal, *J. Alloys Compd.* **625**, 216 (2015)
68. B.J. Rani, M. Ravina, B. Saravanakumar, G. Ravi, V. Ganesh, S. Ravichandran, R. Yuvakkumar, *Nano-Structures and Nano-Objects* **14**, 84 (2018)
69. S. B. Zhang, S. H. Wei, and A. Zunger, *Phys. Rev. B - Condens. Matter Mater. Phys.* **63**, 1 (2001).
70. M. Hashim, A. Ahmed, S.A. Ali, S.E. Shirsath, M.M. Ismail, R. Kumar, S. Kumar, S.S. Meena, D. Ravinder, *J. Alloys Compd.* **834**, 155089 (2020)
71. F. Shahbaz Tehrani, V. Daadmehr, A. T. Rezakhani, R. Hosseini Akbarnejad, and S. Gholipour, *J. Supercond. Nov. Magn.* **25**, 2443 (2012).
72. D.A. Wheeler, G. Wang, Y. Ling, Y. Li, J.Z. Zhang, *Energy Environ. Sci.* **5**, 6682 (2012)
73. M. Hjiri, N.H. Alonizan, M.M. Althubayti, S. Alshammari, H. Besbes, M.S. Aida, *J. Mater. Sci. Mater. Electron.* **30**, 15379 (2019)
74. Z.K. Heiba, M.B. Mohamed, N.G. Imam, *J. Supercond. Nov. Magn. Supercond. Nov. Magn.* **30**, 3123 (2017)
75. R. Chen, J.L. Lawless, V. Pagonis, *Radiat. Meas. Meas.* **46**, 1380 (2011)

76. A. V. Ravindra, M. Chandrika, C. Rajesh, P. Kollu, S. Ju, and S. D. Ramarao, *Eur. Phys. J. Plus* **134**, (2019).
77. W.N. Wang, W. Widiyastuti, T. Ogi, I.W. Lenggoro, K. Okuyama, *Chem. Mater.* **19**, 1723 (2007)
78. M. Siddique, N.M. Butt, *Phys. B Condens. Matter* **405**, 4211 (2010)
79. E. Wieser, W. Meisel, K. Kleinstück, *Phys. Status Solidi* **16**, 127 (1966)
80. A. M. Kumar, K. H. Rao, and J. M. Greneche, *J. Appl. Phys.* **105**, (2009).
81. U. Bhattacharya, V.S. Darshane, *J. Mater. Chem.* **3**, 299 (1993)
82. S.K. Gore, R.S. Mane, M. Naushad, S.S. Jadhav, M.K. Zate, Z.A. Alothman, B.K.N. Hui, *Dalt. Trans.* **44**, 6384 (2015)
83. A. Ghasemi, V. Šepelák, X. Liu, A. Morisako, *J. Appl. Phys.* **107**, 10 (2010)
84. S. Burianova, J. Poltiero Va Vejpravova, P. Holec, J. Plocek, and D. Niznansky, *J. Appl. Phys.* **110**, 073902 (2011).
85. N.S. Gajbhiye, S. Bhattacharyya, G. Balaji, R.S. Ningthoujam, R.K. Das, S. Basak, J. Weissmüller, *Hyperfine Interact.* **165**, 153 (2005)
86. S.M. Patange, S.E. Shirsath, S.S. Jadhav, K.M. Jadhav, *Phys. Status Solidi Appl. Mater. Sci.* **209**, 347 (2012)
87. K. Haneda, *Can. J. Phys.* **65**, 1233 (1987)
88. M. Grigorova, H.J. Blythe, V. Blaskov, V. Rusanov, V. Petkov, V. Masheva, D. Nihitjanova, L.M. Martinez, J.S. Muñoz, M. Mikhov, *J. Magn. Magn. Mater.* **183**, 163 (1998)
89. J. P. Singh, G. Dixit, R. C. Srivastava, H. M. Agrawal, and K. Asokan, *J. Phys. D. Appl. Phys.* **44**, (2011).
90. R. Ramchandra Kiran and T. Patri, *J. Mater. Res. Technol.* **10**, 1169 (2021).
91. P. Pahuja, R.K. Kotnala, R.P. Tandon, *J. Alloys Compd.* **617**, 140 (2014)
92. D.M. Ghone, S. Premkumar, K.K. Patankar, S.D. Kaushik, V.L. Mathe, *Sensors Actuators. A Phys.* **301**, 111716 (2020)

**Publisher's Note** Springer Nature remains neutral with regard to jurisdictional claims in published maps and institutional affiliations.

Springer Nature or its licensor (e.g. a society or other partner) holds exclusive rights to this article under a publishing agreement with the author(s) or other rightsholder(s); author self-archiving of the accepted manuscript version of this article is solely governed by the terms of such publishing agreement and applicable law.